Keller Box and Smoothed Particle Hydrodynamic Numerical Simulation of Two-Phase Transport in Blood Purification Auto-Transfusion Dialysis Hybrid Device with Stokes and Darcy Number Effects

O. Anwar Beg[1,*], B. Vasu[2], T. Sochi[3] and V.R. Prasad[4]

[1]*Gort Engovation Research (Propulsion/Biomechanics), 15 Southmere Ave., Bradford BD7 3NU, UK*

[2]*Department of Mathematics, Motilal Nehru National Institute of Technology, Allahabad, India*

[3]*Department of Physics and Astronomy, University College London, Gower Street, London, UK*

[4]*Department of Mathematics, Madanapalle Institute of Technology and Science, Madanapalle-517325, India*

Abstract: A computational simulation of laminar natural convection fully-developed multi-phase suspension in a porous medium channel is presented. The Darcy model is employed for the porous material which is valid for low velocity, viscous-dominated flows. The Drew-Marble fluid-particle suspension model is employed to simulate both particulate (red blood cell) and fluid (plasma) phases. The transformed two-point nonlinear boundary value problem is shown to be controlled by a number of key dimensionless thermo-physical parameters, namely the Darcy number (Da), momentum inverse Stokes number (Sk_m), particle loading parameter (p_L), inverse thermal Stokes number (Sk_T), particle-phase wall slip parameter (Ω) and buoyancy parameter (B). Detailed numerical solutions are presented with an optimized **K**eller **B**ox implicit finite difference **M**ethod (**KBM**) for the influence of these parameters on the fluid-phase velocity (U) and particle-phase velocity (Up). Validation is also included using the **S**moothed **P**article **H**ydrodynamic (**SPH**) Lagrangian method and excellent correlation achieved. Increasing Darcy number is observed to significantly accelerate the fluid-phase flow and less dramatically enhance particle-phase velocity field. Magnitudes of fluid phase velocity are also elevated with both increasing viscosity ratio and particle-phase wall slip parameter. Increasing buoyancy effect depresses particle phase velocity. An increase in particle loading parameter is also observed to suppress both fluid and particle phase velocities. No tangible change in fluid or particle phase temperatures is computed with increasing Darcy number. The study is relevant to dialysis devices exploiting thermal and porous media filtration features.

Keywords: Biotechnology, blood flow, Prandtl number, two-phase suspension, Stokes number, particle phase velocity, Keller box finite difference algorithm, Smoothed particle hydrodynamics (SPH), Thermo-haemotological processing, autotransfusion medicine, biothermal devices.

1. INTRODUCTION

Multi-phase flows arise frequently in many complex and diverse areas of biophysical transport including blood flow in coronary arteries [1], capillary flows [2], cytoplasm dynamics and cell motion [3], micro-vascular flows [4], renal hydromechanics [5] (two-phase flow of an inner core of rouleaux surrounded by a cell-depleted peripheral layer which manifests with a decrease in hydrodynamic resistance to flow). An excellent review of microvascular applications has been given by Pries *et al.* [6]. The fluid dynamics of two-phase systems has led to significant developments in theoretical models which can capture fluid-particle suspension characteristics, viscosity variation, heat transfer features etc. Many models have been presented including percolation physics [7], generalized Taylor dispersion models [8], spatially-periodic models for porous media [9] and dusty suspension models [10]. The latter have been found to be quite robust in simulating simple *two-phase flows of blood in porous systems*. In these simulations blood is assumed to behave as a two-component mixture comprised of plasma and red blood cells (RBCs). The plasma is assumed to behave as a viscous fluid whereas the RBCs exhibit a granular-like structure where the viscosity also depends on the shear-rate. The dusty model has been employed by Bég *et al.* [11, 12] recently to analyze buoyancy-driven blood flow and heat diffusion in porous media systems using differential transform and homotopy simulation techniques. Allied to these investigations a range of other models for two-phase blood flows have also been developed and these generally aim to mimick the so-called “plasma-skimming phenomenon” and include *edge-core, averaging, immersed particle* and *effective medium* approaches [13]. To simulate two-phase blood flows with any of these models, numerical methods are generally required. Biophysics researchers have generally adopted approaches developed in chemical and petroleum engineering for flows in porous media.

*Address correspondence to this author at the Gort Engovation Research (Propulsion/Biomechanics), 15 Southmere Ave., Bradford BD7 3NU, UK; Tel: +44 01274 504 600; Fax: +44 01274 504 601; E-mail: gortoab@gmail.com

E-ISSN: 2311-1755/13

Important computational techniques developed include finite-element/finite volume mixed algorithms [14], finite difference methods [15] and moving finite element methods [16]. Dzwinel *et al.* [17] deployed a discrete-particle model in 3D to simulate aggregation of red blood cells in plasma flows to simulate scales from 0.001 to 100 μm, achieving significantly finer resolution than classical computational fluid dynamics. The flexible viscoelastic red blood cells and the walls of the elastic vessel are simulated as solid particles held together by elastic harmonic forces and the plasma modelled as a system of dissipative fluid particles. They concluded that aggregation of red blood cells in capillary vessels may be accurately analyzed by depletion forces and hydrodynamic interactions and that the cluster of "sickle" cells formed in the choking point of the capillary efficiently decelerates the flow. Sankar and Lee [18] studied analytically the pulsatile flow of a two-phase model for arterial stenosis hemodynamics, elucidating the influence of periodicity, stenosis, peripheral layer and non-Newtonian behavior of blood. They simulated the blood in the core region as a Herschel-Bulkley fluid and the plasma in the peripheral layer as a Newtonian fluid, and utilized a perturbation method, observing that the plug core radius and resistance to flow increase as the stenosis size increases while wall shear stress increases with the increase of yield stress. Bourantas *et al.* [19] investigated two-phase blood flow behavior and the effect of hemodynamic pulsation on the distributions of luminal surface of low density lipoproteins (LDL) concentration and oxygen flux along the wall of the human aorta. They compared the predictions of a two-phase model with those of the single phase one under both steady flow and realistic pulsatile flow conditions using a human aorta model constructed from CT images, emphasizing the need to address mass transfer of low-density lipoproteins (LDLs) which arises in the arterial system in the localization of atherogenesis. They simulated a tapered aorta in order to stabilize the flow of blood, and effectively delayed the attenuation of the helical flow, forcing blood to flow past the arch and into the first part of the descending aorta, showing that the analysis may expound why the ascending aorta and the arch are relatively free of atherosclerosis. The dependence of viscosity and diffusivity on the local density was incorporated in the two-phase flow model rendering these quantities position-dependent. Furthermore for oxygen transport, they compared the numerical results obtained with those utilizing the shear thinning non-Newtonian nature of blood and also examined the effect of pulsatile flow on the transport of LDLs and on the oxygen flux in the aorta. Federspiel [20] studied theoretically the effect of particulate (two-phase) nature of blood on pulmonary oxygen exchange. Red cells were simulated as discrete hemoglobin (Hb) containing spheres flowing in single file suspension through a cylindrical capillary surrounded by a uniform annulus of alveolar tissue. The model accurately represented free diffusion of O_2 from alveolar air space through tissue and plasma, free and Hb facilitated diffusion of O_2 inside red cells, and the intracellular kinetics of O_2-Hb binding. Oxygen uptake was driven by a specified O_2 tension at the alveolar surface. The computed pulmonary diffusing capacity (DL_{O2}) was observed to fall with increasing spacing (LS) between red cells. The reduction in DL_{O2} with increasing LS was marshalled more by a reduction in membrane diffusing capacity (DM_{O2}), than by the reduction in erythrocyte diffusing capacity (De_{O2}). The dependence of DM_{O2} on cell spacing was attributed to the manner in which O_2 flowed across the alveolar surface into the discrete sinks (red cells) within the capillaries. Further applications of two-phase blood flow in porous media include haemodialysis and filtration devices. As the most widely used blood purification method, hemodialysis serves as a replacement for renal detoxification and discharge functions in the event of chronic kidney failure. The patient's blood is routed *via* a vessel access point by means of a blood pump through a bloodline system into the dialyser (artificial kidney). This is where the blood is effectively purified. The blood flows through the dialyser'scapillaries, while the dialyser liquid is bypassed outside the capillary walls in the direction opposing the flow of blood. The capillary walls are semi-permeable, i.e. they permit an exchange of substances between the blood and dialyser liquid [21]. The primary transport mechanism during hemodialysis is selective diffusion. The size of the semi-permeable capillary walls' pores determines which molecules are able to diffuse from the blood into the dialyser liquid and vice versa. The capillary walls can be permeated by small and medium-sized molecules and water, but not by blood cells or large molecules, e.g. proteins. This eliminates toxic substances, restores normal concentrations of other substances (e.g. electrolytes such as potassium, sodium and calcium), balances the blood pH value and removes excess water which has accumulated in the body. While individual substances are eliminated mainly by diffusion, the water is filtered by the capillary walls' semi-permeable membrane out of the blood and into the dialyser liquid (ultrafiltration). This is made possible by the positive pressure on the

blood's side and the negative pressure on the dialyser liquid's side (trans-membrane pressure, TMP).

In recent years interest in thermal-dialysis devices and thermal filtration devices for purification and separation of blood suspensions has grown. In the present study we present a viscous-dominated, two-phase model for blood flow and heat transfer under buoyancy forces in a porous media filtration device. The *Drew-Marble fluid-particle suspension model is employed to simulate both particulate (red blood cell) and fluid (plasma) phase*. The boundary value problem is non-dimensionalized and then solved subject to relevant boundary conditions with an optimized Keller box finite difference technique (**KBM**) [22]. Validation is achieved with a smoothed particle hydrodynamic (**SPH**) code [23]. We investigate the effects of momentum Stokes number, Darcy number (biological permeability parameter), Grashof number (free convection i.e. thermal buoyancy parameter) and particle loading parameter, on fluid and particulate phase velocity components and also temperatures. Extensive details

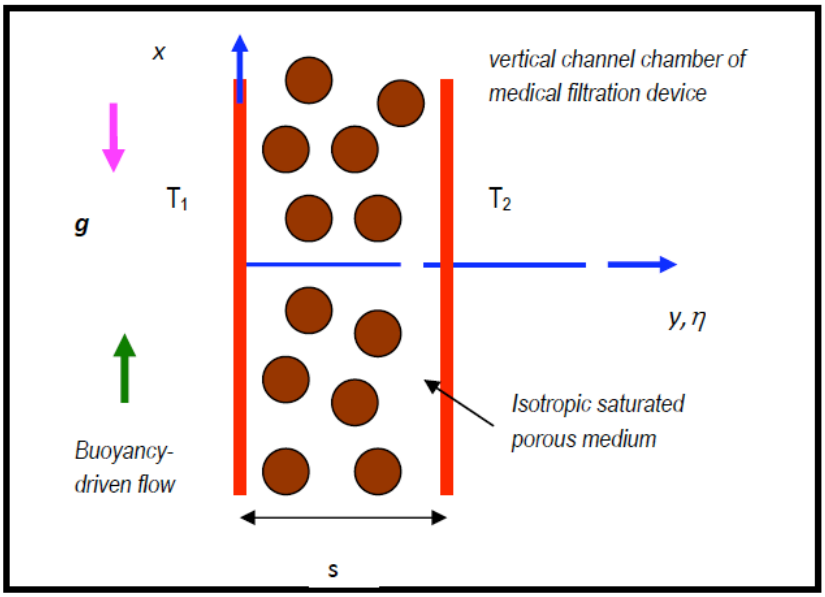

a

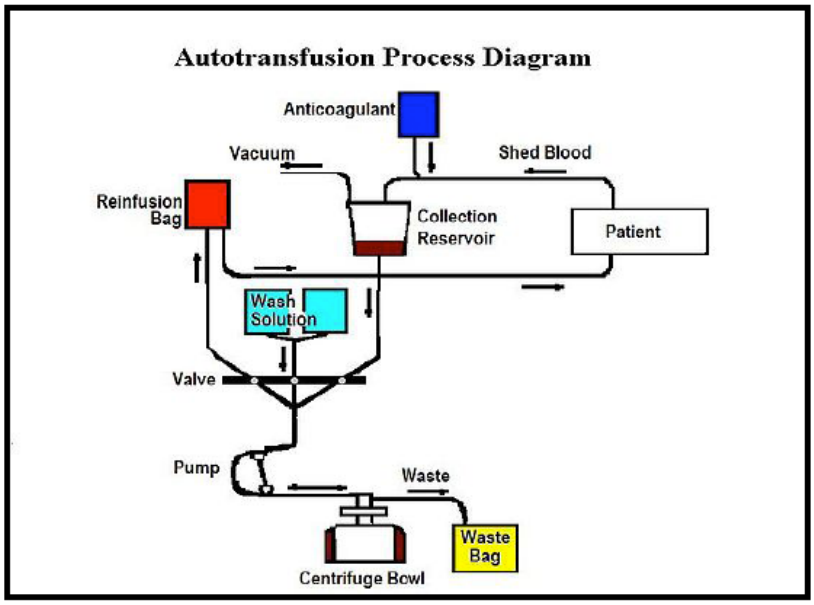

b

Figure 1: a: Idealized 2-D model for biofluid-particle flow regime and coordinate system for the blood filtration component of an auto-transfusion system for medical treatment.

b: Complete autotransfusion process for dialysis patients- filtration device component indicated by re-infusion bag (red box).

of both computational methods are provided. The present study, to the authors' knowledge, is the first to consider coupled fluid-particle suspension flow and heat transfer in a Darcian porous medium vertical chamber. It is relevant to biotechnology and medical engineering haemotological processing systems [24, 25].

2. MATHEMATICAL MODEL

We investigate the coupled momentum and thermal diffusion in fully-developed hemodynamic transport of a fluid-particle (two-phase) suspension in a vertical parallel-plate channel chamber of a haematological filtration device. The chamber contains an isotropic, homogenous porous medium, with the plates separated by a distance, *s*. The regime is in local thermal equilibrium and is illustrated in Figure **1a**. A practical device from the medical industry utilized for hemodynamic filtration is shown in Figure **1b**.

Many of the newest autotransfusion machines are programmable to provide separation of blood into three groups; red cells, platelet poor plasma, and platelet rich plasma. Blood can be drawn from the patient just prior to surgery and then separated. The separated blood components which have been sequestered can be stored during the surgical procedure. The red cells and platelet poor plasma can be given back to the patient through intravenous transfusion during or after surgery. The platelet rich plasma can be mixed with calcium and thrombin to create a product known as autologous platelet gel. The particle phase simulates erythrocytes or other suspensions, which are assumed rigid. The fluid-phase represents plasma. The model is used to simulate a porous medium thermo-bio-filtration device known as a re-infusion bag or box (see Figure **1a**, red box component). This procedure aims to minimize hemolysis and also extract larger bacterial and contaminants from donored blood. It also eliminates clots and clusters. The regime studied employs an x-y coordinate system. The x-direction is directed upwards along the vertical center-line of the channel with the y-direction orientated perpendicular to this. Tortuosity, stratification and thermal dispersion effects are ignored. The channel is infinitely longer than it is wide (the chamber is quite slender, and the flow under this approximation may be considered to be one-dimensional. The number density of the particles is constant throughout the flow. The hydrodynamic and particle phases are modeled as *two interacting continua* and this interaction is confined to the interphase drag force (simulated using a Stokesian linear drag force model) and the interphase heat transfer. The volume fraction of suspended particles is finite and constant. Furthermore the particle-phase pressure is vanishingly small and the particles (erythrocytes) are effectively dragged along with the fluid phase, under natural convection currents (buoyancy forces). The concentration of the particles is assumed to be somewhat low and the suspension is considered dilute in the sense that no *particle-particle interactions* exist. This means that the particle phase is considered *inviscid*. Further details are provided by Drew [26]. The drag forces generated by the filtration medium fibers in the porous matrix are simulated with a linear (Darcy force) and second-order (Forchheimer drag) *via* the *Darcy-Forchheimer* drag force model, following Bég *et al.* [27-30]. The vectorial equations for a two-phase bio-suspension [26, 31] may be shown to take the form:

Fluid Phase (Plasma)

Conservation of mass:

$$\nabla(\rho V) = 0 \tag{1}$$

Conservation of translation momentum:

$$\rho V.\nabla = -\nabla P + \nabla(\mu \nabla V) - \rho_p N(V - V_p) + \rho g - \frac{\mu}{K^*} V \tag{2}$$

Conservation of energy:

$$\rho c V.\nabla T = \nabla(K \nabla T) \rho_p c_p N_T (T_p - T) \tag{3}$$

Particle Phase (Erythrocytes)

Conservation of mass:

$$\nabla(\rho_p V_p) = 0 \tag{4}$$

Conservation of translation momentum:

$$\rho_p V_p.\nabla V_p = \rho_p N(V - V_p) + \rho_p g \tag{5}$$

Conservation of energy:

$$\rho_p c_p V.\nabla T_p = -\rho_p c_p N_T (T_p - T) \tag{6}$$

We eliminate the longitudinal pressure gradient term, from the fluid-phase momentum equation, by re-defining the transport equations at a reference point within the channel. We employ the classical Boussinesq approximation and following definitions:

$$u = 0, T = T_0, \rho = \rho_0, \mu = \mu_0, \mu_p = \mu_{p0},$$
$$T_p = T_{p0}, \rho_p = \rho_{p0}, \mu_p = \mu_{p0} \quad (7)$$

The governing transport equations may be contracted to the following linear ordinary differential equation system, which represent *fluid phase and particle phase momentum* and *energy transfer* incorporating porous media drag forces for the infinite vertical channel, depicted in Figure **1a**:

$$\frac{\mu_0}{\rho_0}\frac{d^2u}{dy^2} + g\beta^*(T - T_0) - \frac{\rho_{p0}}{\rho_0}N(u - u_p) - \frac{\rho_{p0}}{\rho_0}g - \frac{\mu_0}{\rho_0 K^*}u = 0 \quad (8)$$

$$K\frac{d^2T}{dy^2}\rho_p c_p N_T(T_p - T) = 0 \quad (9)$$

$$\mu_p\frac{d^2u_p}{dy^2} + \rho_p N(u - u_p) - \rho_p g = 0 \quad (10)$$

$$\rho_p c_p N_T(T_p - T) = 0 \quad (11)$$

where all parameters have been defined in the nomenclature. The first term in eqn. (8) is the *viscous shear term*, the second is the *thermal buoyancy*, the third is the *fluid-particle coupling term*, the fourth is the *gravity (density ratio) term*. The last term on the left hand side of Eq. (8) is the *Darcian bulk porous media impedance drag*. The conservation of mass in both phases is also identically satisfied. The boundary conditions are defined as follows at the channel walls:

For the Fluid Phase

$$u(0) = u(s) = 0, T(0) = T_1, T(s) = T_2 \quad (12a)$$

For the Particle Phase

$$up(0) = \omega\frac{du_p(0)}{dy} - \frac{g}{N}, u_p(s) = -\omega\frac{du_p(s)}{dy} - \frac{g}{N} \quad (12b)$$

The fluid velocity boundary conditions (12a) correspond to *no-slip* conditions for the fluid phase at the channel walls. Since the particle phase may resemble a rarefied gas and undergoes slip at a boundary, it is feasible to adopt such a boundary condition for hemodynamic inter-particle slip. The model developed therefore constitutes a robust, well-posed, two-point nonlinear boundary value problem for viscous-dominated thermofluid transport. The model may be normalized by introducing the following non-dimensional variables:

$$y = s\eta, u = \frac{\mu}{\rho_s}U, u_p = \frac{\mu}{\rho s}U_p, T = [T_2 - T_0]\Phi + T_0, T_0 = \frac{[T_1 + T_2]}{2},$$
$$T_p = [T_2 - T_0]\Phi_p + T_0, Da = \frac{K^*}{s^2}, \mathrm{Pr} = \frac{\mu c}{k}, \gamma = \frac{c_p}{c}, Sk_T = \frac{\rho N_T s^2}{\mu},$$
$$Sk_m = \frac{\rho N s^2}{\mu}, P_L = \frac{\rho_p}{\rho}, B = \frac{\rho g s^3}{\mu^2}\Lambda = \frac{\mu_p}{k\mu}, Gr = \frac{g\beta^*\rho^2 s^3[T_2 - T_0]}{\mu^2} \quad (13)$$

The dimensionless conservation equations reduce to the final form:

$$\frac{d^2U}{d\eta^2} + Gr\Phi - Sk_m P_L(U - U_p) - P_L B - \frac{1}{Da}U = 0 \quad (14)$$

$$\frac{1}{\mathrm{Pr}}\frac{d^2\Phi}{d\eta^2} + Sk_T\gamma P_L(\Phi_p - \Phi) = 0 \quad (15)$$

$$\Lambda\frac{d^2U_p}{d\eta^2} + Sk_m(U - U_p) + B = 0 \quad (16)$$

$$Sk_T(\Phi_p - \Phi) = 0 \quad (17)$$

The transformed dimensionless boundary conditions are:

For the Fluid Phase

$$U(0) = U(1) = 0, \Phi(0) = -1, \Phi(1) = 1 \quad (18)$$

For the Particle Phase

$$U_p(0) = \Omega\frac{dU_p(0)}{d\eta} - \frac{B}{sk_m} \quad (19)$$

$$U_p(1) = -\Omega\frac{dU_p(1)}{d\eta} - \frac{B}{sk_m} \quad (20)$$

The parameter, Ω, i.e. the dimensionless particle-phase wall slip parameter, simulates the effects of wall slip on the flow and heat transfer in the regime. The parameters N and N_T which feature in the inverse momentum Stokes number (Sk_m) and inverse temperature Stokes number (Sk_T), respectively, are measures of relaxation times. The non-dimensional boundary value problem (**BVP**) defined by eqns. (14)-(17) with boundary conditions (18-20) is solved using two numerical methods- the **K**eller **b**ox implicit finite difference second order accurate **m**ethod (**KBM**) and the **s**moothed **p**article **h**ydrodynamic (**SPH**) technique. Extensive visualization of the response of the multi-phase velocity and temperature distributions to variation in the key biophysical parameters arising in the model is presented.

3. NUMERICAL SOLUTION WITH KELLER BOX METHOD (KBM)

As described in Cebeci and Bradshaw [32, 33], Vasu *et al.* [34], Keller [35] and Bég [36] and Prasad *et al.* [37-39], the differential equations (13) to (16) subject to the boundary conditions (17a and b) are first written as a system of first-order equations. For this purpose, we introduce new dependent variables:

$$u(=U),\ g(=\Phi),\ s(=U_p),\ z(=\Phi_p)\ \text{and}$$
$$v(=U'),\ p(=\Phi'),\ t(=U_p'),\ m(=\Phi_p') \tag{21}$$

These signify the variables for velocities and temperature respectively. Therefore, we obtain the following eight first-order equations:

$$u' = v \tag{22}$$

$$g' = p \tag{23}$$

$$s' = t \tag{24}$$

$$z' = m \tag{25}$$

$$v' + Gr\ g - Sk_m P_L (u - s) - P_L B - \frac{1}{Da} u = 0 \tag{26}$$

$$\frac{p'}{\Pr} + Sk_T \gamma P_L (z - g) = 0 \tag{27}$$

$$\Lambda t' + Sk_m (u - s) + B = 0 \tag{28}$$

$$Sk_T m' - Sk_T p' = 0$$

Where primes denote differentiation with respect to η. In terms of the dependent variables, the boundary conditions become:

$$\eta = 0: \quad u = 0, \quad g = -1, \quad z = -1, \quad s = \Omega t(0) - \frac{B}{Sk_m}$$
$$\eta = 1: \quad u = 0, \quad g = 1, \quad z = 1, \quad s = -\Omega t(1) - \frac{B}{Sk_m} \tag{29}$$

We now write the difference equations that are to approximate equations (22-28) by considering one "Keller box" mesh rectangle as in Figure **2**.

We start by writing the finite-difference approximations of the ordinary differential equations using centered-difference derivatives. This leads to:

$$\frac{(u_j^u - u_{j-1}^n)}{h_j} = \frac{1}{2}(v_j^n + v_{j-1}^n) = v_{j-1/2,}^n \tag{30}$$

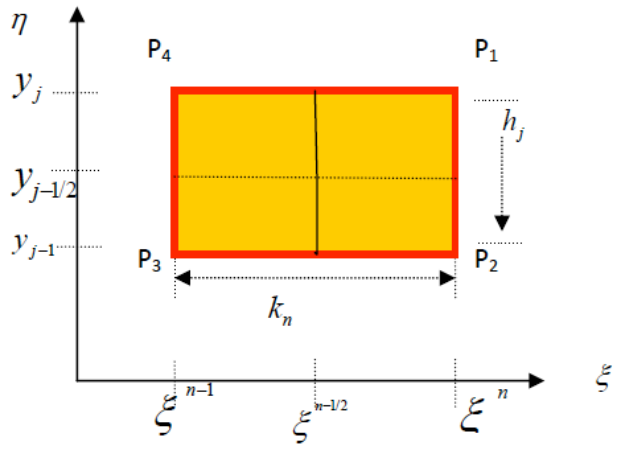

Figure 2: "Keller-Box" cell for finite difference approximation.

$$\frac{(g_j^u - g_{j-1}^n)}{h_j} = \frac{1}{2}(p_j^n + p_{j-1}^n) = p_{j-1/2,}^n \tag{31}$$

$$\frac{(s_j^u - s_{j-1}^n)}{h_j} = \frac{1}{2}(t_j^n + t_{j-1}^n) = t_{j-1/2,}^n \tag{32}$$

$$\frac{(z_j^u - z_{j-1}^n)}{h_j} = \frac{1}{2}(m_j^n + m_{j-1}^n) = m_{j-1/2,}^n \tag{33}$$

$$\left(\frac{(v_j^u - v_{j-1}^n)}{h_j}\right) + Grg_{j-1/2}^n - Sk_m P_L\left[(u)_{j-1/2}^n - (s)_{j-1/2}^n\right] - \left(\frac{1}{Da}\right) u_{j-1/2}^n$$
$$= -\left[(v') + Gr\ g - Sk_m P_L (u - s) - P_L B\left(\frac{1}{Da}\right) u\right]_{j-1/2}^{n-1} \tag{34}$$

$$\frac{1}{\Pr}\left(\frac{p_j^n - p_{j-1}^n}{h_j}\right) + Sk_T \gamma P_L (z)_{j-1/2}^n - Sk_T \gamma P_L (g)_{j-1/2}^n$$
$$= -\left[\frac{1}{\Pr}(p') + Sk_T \gamma P_L (z - g)\right]_{j-1/2}^{n-1} \tag{35}$$

$$\Lambda\left[\frac{t_j^n - t_{j-1}^n}{h_j}\right] + Sk_m (u)_{j-1/2}^n - Sk_m (s)_{j-1/2}^n$$
$$= -\left[\Lambda(t') + Sk_m (u) - Sk_m (s)\right]_{j-1/2}^{n-1} \tag{36}$$

$$Sk_T\left(\frac{m_j^n - m_{j-1}^n}{h_j}\right) + Sk_T\left(\frac{p_j^n - p_{j-1}^n}{h_j}\right)$$
$$= -\left[Sk_T (m') + Sk_T (p')\right]_{j-1/2}^{n-1} \tag{37}$$

Equations (30)-(37) are imposed for *j= 1, 2… J* at given *n*. At $\xi = \xi^n$, the boundary conditions (29) become:

$$u_0^n = 0, \quad g_0^n = -1, \quad z_0^n = -1, \quad s_0^n = \Omega t_0^n - \frac{B}{Sk_m}$$
$$u_j^n = 0, \quad g_j^n = 0, \quad z_j^n = 0, \quad s_j^n = -\Omega t_j^n - \frac{B}{Sk_m} \tag{38}$$

Newton's Method

If we assume $u_j^{n-1}, v_j^{n-1}, g_j^{n-1}, p_j^{n-1}, s_j^{n-1}, t_j^{n-1}, z_j^{n-1}, m_j^{n-1}$ to be known for $0 \le j \le J$, then equations (30) to (37) are a system of equations for the solution of the unknowns $\left(u_j^n, v_j^n, g_j^n, p_j^n, s_j^n, t_j^n, z_j^n, m_j^n\right)$, j = 0, 1, 2…J. For simplicity of notation we shall write the unknowns at $\xi = \xi^n$ as $\left(u_j^n, v_j^n, g_j^n, p_j^n, s_j^n, t_j^n, z_j^n, m_j^n\right) \equiv \left(u_j, v_j, g_j, p_j, s_j, t_j, z_j, m_j\right)$ Then the system of equations (30) to (37) can be written as (after multiplying with h_j)

$$u_j - u_{j-1} - \frac{h_j}{2}(v_j + v_{j-1}) = 0, \tag{39}$$

$$g_j - g_{j-1} - \frac{h_j}{2}(p_j + p_{j-1}) = 0, \tag{40}$$

$$s_j - s_{j-1} - \frac{h_j}{2}(t_j + t_{j-1}) = 0, \tag{41}$$

$$z_j - z_{j-1} - \frac{h_j}{2}(m_j + m_{j-1}) = 0, \tag{42}$$

$$\left(v_j^n - v_{j-1}^n\right) + \frac{h_j}{2} Gr(g_j^n + g_{j-1}^n) - \frac{h_j}{2} Sk_m P_L$$
$$\left[\left(u_j^n + u_{j-1}^n\right) - \left(s_j^n + s_{j-1}^n\right)\right] - \frac{h_j}{2}\left(\frac{1}{Da}\right)\left(u_j^n + u_{j-1}^n\right) = [R_1]_{j-1/2}^{n-1} \tag{43}$$

$$\frac{1}{\Pr}(p_j^n - p_{j-1}^n) + \frac{h_j}{2} Sk_T \gamma P_L (z_j^n + z_{j-1}^n)$$
$$- \frac{h_j}{2} Sk_T \gamma P_L (g_j^n + g_{j-1}^n) = [R_2]_{j-1/2}^{n-1} \tag{44}$$

$$\Lambda(t_j^n - t_{j-1}^n) + \frac{h_j}{2} Sk_m (u_j^n + u_{j-1}^n)$$
$$- \frac{h_j}{2} Sk_m (s_j^n + s_{j-1}^n) = [R_3]_{j-1/2}^{n-1} \tag{45}$$

$$Sk_T (m_j^n - m_{j-1}^n) + Sk_T (p_j^n + p_{j-1}^n) = [R_4]_{j-1/2}^{n-1} \tag{46}$$

Where

$$[R_1]_{j-1/2}^{n-1} =$$
$$-h_j\left[\left(\frac{v_j - v_{j-1}}{h_j}\right) + Gr\, g - Sk_m P_L (u - s) - P_L B - \left(\frac{1}{Da}\right)u\right]_{j-1/2}^{n-1} \tag{47}$$

$$[R_2]_{j-1/2}^{n-1} = -h_j\left[\frac{1}{\Pr}\left(\frac{p_j - p_{j-1}}{h_j}\right) + Sk_T \gamma P_L (z - g)\right]_{j-1/2}^{n-1} \tag{48}$$

$$[R_3]_{j-1/2}^{n-1} = -h_j\left[\Lambda\left(\frac{t_j - t_{j-1}}{h_j}\right) + Sk_m(u) - Sk_m(s)\right]_{j-1/2}^{n-1} \tag{49}$$

$$[R_4]_{j-1/2}^{n-1} = -h_j\left[Sk_T\left(\frac{m_j - m_{j-1}}{h_j}\right) + Sk_T\left(\frac{p_j - p_{j-1}}{h_j}\right)\right]_{j-1/2}^{n-1} \tag{50}$$

$[R_1]_{j-1/2}^{n-1}$, $[R_2]_{j-1/2}^{n-1}$, $[R_3]_{j-1/2}^{n-1}$ and involve only know $[R_4]_{j-1/2}^{n-1}$ quantities if we assume that solution is known on $\xi = \xi^{n-1}$. To solve equation (39) to (46) with (40) by Newton's method, we introduce the iterates $\left[u_j^{(i)}, v_j^{(i)}, g_j^{(i)}, p_j^{(i)}, s_j^{(i)}, t_j^{(i)}, z_j^{(i)}, m_j^{(i)}\right]$, i = 0, 1, 2…

To linearize the nonlinear system of equations (39) to (46) using Newton's method, we introduce the following iterates

$$\begin{aligned} u_j^{(i+1)} &= u_j^{(i)} + \delta u_j^{(i)}, \quad & v_j^{(i+1)} &= v_j^{(i)} + \delta v_j^{(i)}, \\ g_j^{(i+1)} &= g_j^{(i)} + \delta g_j^{(i)}, \quad & p_j^{(i+1)} &= p_j^{(i)} + \delta p_j^{(i)}, \\ s_j^{(i+1)} &= s_j^{(i)} + \delta s_j^{(i)}, \quad & t_j^{(i+1)} &= t_j^{(i)} + \delta t_j^{(i)}, \\ z_j^{(i+1)} &= z_j^{(i)} + \delta z_j^{(i)}, \quad & m_j^{(i+1)} &= m_j^{(i)} + \delta m_j^{(i)}, \end{aligned} \tag{51}$$

Then we substitute these expressions into equations (39) to (43) and this yields

$$\left(u_j^{(i)} + \delta u_j^{(i)}\right) - \left(u_{j-1}^{(i)} + \delta u_{j-1}^{(i)}\right) - \frac{h_j}{2}\left(v_j^{(i)} + \delta v_j^{(i)} + v_{j-1}^{(i)} + \delta v_{j-1}^{(i)}\right) = 0, \tag{52}$$

$$\left(g_j^{(i)} + \delta g_j^{(i)}\right) - \left(g_{j-1}^{(i)} + \delta g_{j-1}^{(i)}\right) - \frac{h_j}{2}\left(g_j^{(i)} + \delta g_j^{(i)} + g_{j-1}^{(i)} + \delta g_{j-1}^{(i)}\right) = 0, \tag{53}$$

$$\left(s_j^{(i)} + \delta s_j^{(i)}\right) - \left(s_{j-1}^{(i)} + \delta s_{j-1}^{(i)}\right) - \frac{h_j}{2}\left(t_j^{(i)} + \delta t_j^{(i)} + t_{j-1}^{(i)} + \delta t_{j-1}^{(i)}\right) = 0, \tag{54}$$

$$\left(z_j^{(i)} + \delta z_j^{(i)}\right) - \left(z_{j-1}^{(i)} + \delta z_{j-1}^{(i)}\right) - \frac{h_j}{2}\left(m_j^{(i)} + \delta m_j^{(i)} + m_{j-1}^{(i)} + \delta m_{j-1}^{(i)}\right) = 0, \tag{55}$$

$$(v_j^{(i)} + \delta v_j^{(i)}) - (v_{j-1}^{(i)} + \delta v_{j-1}^{(i)}) + \frac{hj}{2} Gr(g_j^{(i)} + \delta g_j^{(i)} + g_{j-1}^{(i)} + \delta g_{j-1}^{(i)})$$

$$-\frac{h_j}{2}Sk_m P_L\left[(u_j^{(i)}+\delta u_j^{(i)}+u_{j-1}^{(i)}+\delta u_{j-1}^{(i)})-(s_j^{(i)}+\delta s_j^{(i)}+s_{j-1}^{(i)}+\delta s_{j-1}^{(i)})\right]$$
$$-\frac{h_j}{2}\left(\frac{1}{Da}\right)(u_j^{(i)}+\delta u_j^{(i)}+u_{j-1}^{(i)}+\delta u_{j-1}^{(i)})=[R_1]_{j-1/2}^{n-1} \quad (56)$$

$$\frac{1}{\Pr}\left[(p_j^{(i)}+\delta p_j^{(i)})-(p_{j-1}^{(i)}+\delta p_{j-1}^{(i)})\right]$$
$$+\frac{hj}{2}Sk_T\gamma P_L\left[(z_j^{(i)}+\delta z_j^{(i)})+(z_{j-1}^{(i)}+\delta z_{j-1}^{(i)})\right] \quad (57)$$
$$-\frac{h_j}{2}Sk_T\gamma P_L\left[(g_j^{(i)}+\delta g_j^{(i)})+(g_{j-1}^{(i)}+\delta g_{j-1}^{(i)})\right]=[R_2]_{j-1/2}^{n-1}$$

$$\Lambda\left[(t_j^{(i)}+\delta t_j^{(i)})-(t_{j-1}^{(i)}+\delta t_{j-1}^{(i)})\right]$$
$$+\frac{hj}{2}Sk_m\left[(u_j^{(i)}+\delta u_j^{(i)})+(u_{j-1}^{(i)}+\delta u_{j-1}^{(i)})\right] \quad (58)$$
$$-\frac{h_j}{2}Sk_m\left[(s_j^{(i)}+\delta s_j^{(i)})+(s_{j-1}^{(i)}+\delta s_{j-1}^{(i)})\right]=[R_3]_{j-1/2}^{n-1}$$

$$Sk_T\left[(m_j^{(i)}+\delta m_j^{(i)})-(m_{j-1}^{(i)}+\delta m_{j-1}^{(i)})\right]$$
$$+Sk_T\left[(p_j^{(i)}+\delta p_j^{(i)})-(p_{j-1}^{(i)}+\delta p_{j-1}^{(i)})\right]=[R_4]_{j-1/2}^{n-1} \quad (59)$$

Next we drop the terms that are quadratic in $\left(\delta u_j^{(i)},\delta v_j^{(i)},\delta g_j^{(i)},\delta p_j^{(i)},\delta s_j^{(i)},\delta t_j^{(i)},\delta z_j^{(i)},\delta m_j^{(i)}\right)$.

We have also dropped the superscript *i* for simplicity. After some algebraic manipulations, the following linear tri-diagonal system of equations is obtained:

$$\delta u_j-\delta u_{j-1}-\frac{h_j}{2}(\delta v_j+\delta v_{j-1})=(r_1)_{j-1/2}, \quad (60)$$

$$\delta g_j-\delta g_{j-1}-\frac{h_j}{2}(\delta p_j+\delta p_{j-1})=(r_2)_{j-1/2}, \quad (61)$$

$$\delta s_j-\delta s_{j-1}-\frac{h_j}{2}(\delta t_j+\delta t_{j-1})=(r_3)_{j-1/2}, \quad (62)$$

$$\delta z_j-\delta z_{j-1}-\frac{h_j}{2}(\delta m_j+\delta m_{j-1})=(r_4)_{j-1/2}, \quad (63)$$

$$(a_1)_j\delta v_j+(a_2)_j\delta v_{j-1}+(a_3)_j\delta u_j+(a_4)_j\delta u_{j-1}$$
$$+(a_5)_j\delta_{gj}+(a_6)_j\delta g_{j-1}+(a_7)_j\delta s_j+(a_8)_j\delta s_{j-1}=(r_5)_{j-1/2}, \quad (64)$$

$$(b_1)_j\delta p_j+(b_2)_j\delta p_{j-1}+(b_3)_j\delta g_j+(b_4)_j\delta g_{j-1}$$
$$+(b_5)_j\delta z_j+(b_6)_j\delta z_{j-1}=(r_6)_{j-1/2}, \quad (65)$$

$$(c_1)_j\delta t_j+(c_2)_j\delta t_{j-1}+(c_3)_j\delta u_j+(c_4)_j\delta u_{j-1}$$
$$+(c_5)_j\delta s_j+(c_6)_j\delta s_{j-1}=(r_7)_{j-1/2}, \quad (66)$$

$$(d_1)_j\delta m_j+(d_2)_j\delta m_{j-1}+(d_3)_j\delta p_j+(d_4)_j\delta p_{j-1}=(r_8)_{j-1/2}, \quad (67)$$

Where

$$(a_1)_j=1,\quad (a_2)_j=-1,(a_3)_j=-\frac{h_j}{2}Sk_m P_L-\frac{h_j}{2}\left(\frac{1}{Da}\right),$$
$$(a_4)_j=(a_3)_j,$$
$$(a_5)_j=\frac{h_j}{2}Gr,\quad (a_6)_j=(a_5)_j,(a_7)_j=\frac{h_j}{2}Sk_m P, \quad (68)$$
$$(a_8)_j=(a_7)_j,$$

$$(b_1)_j=\frac{1}{\Pr},\quad (b_2)_j=-\frac{1}{\Pr},(b_3)_j=-\frac{h_j}{2}Sk_T\gamma P_L,\quad (b_4)_j=(b_3)_j,$$
$$(b_5)_j=\frac{h_j}{2}Sk_T\gamma P_L,\qquad (b_6)_j=(b_5)_j, \quad (69)$$

$$(c_1)_j=\Lambda,\quad (c_2)_j=-\Lambda,(c_3)_j=\frac{h_j}{2}Sk_m,(c_4)_j$$
$$=(c_3)_j,(c_5)_j=-\frac{h_j}{2}Sk_m,(c_6)_j=(c_5)_j, \quad (70)$$

$$(d_1)_j=SK_T,\quad (d_2)_j=-Sk_T,\quad (d_3)_j=-Sk_T,\quad (d_4)_j=Sk_T, \quad (71)$$

$$\left.\begin{aligned}
&(r_1)_{j-1/2}=u_{j-1}-u_j+h_j v_{j-1/2},\quad (r_2)_{j-1/2}=g_{j-1}-g_j+h_j p_{j-1/2},\\
&(r_3)_{j-1/2}=s_{j-1}-s_j+h_j t_{j-1/2},\quad (r_4)_{j-1/2}=z_{j-1}-z_j+h_j m_{j-1/2},\\
&(r_5)_{j-1/2}=(v_{j-1}-v_j)-h_j Gr\,g_{j-1/2}+Sk_m P_L h_j\left[(u)_{j-1/2}-(s)_{j-1/2}\right]\\
&-h_j\left(\frac{1}{Da}\right)u_{j-1/2}+(R1)_{j-1/2}^{n-1},\\
&(r_6)_{j-1/2}=\frac{1}{\Pr}(p_{j-1}-p_j)+h_j Sk_T\gamma P_L(z)_{j-1/2}\\
&-h_j Sk_T\gamma P_L(g)_{j-1/2}+(R_2)_{j-1/2}^{n-1},\\
&(r_7)_{j-1/2}=\Lambda(t_{j-1}-t_j)+h_j Sk_m(u)_{j-1/2}\\
&-h_j Sk_m(s)_{j-1/2}+(R_3)_{j-1/2}^{n-1},
\end{aligned}\right\}$$
$$(r_8)_{j-1/2}=Sk_T(m_{j-1}-m_j)+Sk_T(p_j-p_{j-1})+(R_4)_{j-1/2}^{n-1} \quad (72)$$

To complete the system (63)-(67), we recall the boundary conditions (38), which can be satisfied exactly with no iteration [33]. Therefore to maintain these correct values in all the iterates, we take:

$$\delta u_0=0,\quad \delta s_0^n=0,\quad \delta g_0=0,\quad \delta z_0=0,$$
$$\delta u_J=0,\quad \delta s_J=0,\quad \delta g_J=0,\quad \delta z_J=0 \quad (73)$$

Block-Elimination method

To linear system (60)-(67) can now be solved by the block-elimination method as outlined in Bég [36] and

Vasu *et al.* [34]. The linearized difference equations of the system (56)-(63) have a block-tri-diagonal structure. Commonly, the *block tri-diagonal structure* consists of variables or constants; however in the Keller box method, it consists of block matrices. Before we can proceed further with the block-elimination method, we demonstrate how to derive the elements of the block matrices from the linear system (60)-(64). We consider three cases, namely when *j = 1, J-1* and *J.*

When j = 1, the linear systems (22-25) become:

$$\left.\begin{aligned}
\delta u_1 - \delta u_0 - \frac{h_j}{2}(\delta v_1 + \delta v_0) &= (r_1)_{1-1/2},\\
\delta g_1 - \delta g_0 - \frac{h_j}{2}(\delta p_1 + \delta p_0) &= (r_2)_{1-1/2},\\
\delta s_1 - \delta s_0 - \frac{h_j}{2}(\delta t_1 + \delta t_0) &= (r_3)_{1-1/2},\\
\delta z_1 - \delta z_0 - \frac{h_j}{2}(\delta m_1 + \delta m_0) &= (r_4)_{1-1/2},\\
(a_1)_1\delta v_1 + (a_2)_1\delta v_0 + (a_3)_1\delta u_1 + (a_4)_1\delta u_0 + (a_5)_1\delta g_1 &\\
+(a_6)_1\delta g_0 + (a_7)_1\delta s_1 + (a_8)_1\delta s_0 &= (r_5)_{1-1/2,}\\
(b_1)_1\delta p_1 + (b_2)_1\delta p_0 + (b_3)_1\delta g_1 + (b_4)_1\delta g_0 + (b_5)_1\delta z_1 &\\
+(b_6)_1\delta z_0 &= (r_6)_{1-1/2,}\\
(c_1)_1\delta t_1 + (c_2)_1\delta t_0 + (c_3)_1\delta u_1 + (c_4)_1\delta u_0 + (c_5)_1\delta s_1 &\\
+(c_6)_1\delta s_0 &= (r_7)_{1-1/2,}\\
(d_1)_1\delta m_1 + (d_2)_1\delta m_0 + (d_3)_1\delta p_1 + (d_4)_1\delta p_0 &= (r_8)_{1-1/2,}
\end{aligned}\right\} \quad (74)$$

The corresponding matrix form is

(We $d_1 = -\frac{1}{2}h_1$, and $\delta u_0 = 0, \delta s_0^n = 0, \delta g_0 = 0, \delta z_0 = 0$ let from (74)):

$$\begin{bmatrix}
d_1 & 0 & 0 & 0 & d_1 & 0 & 0 & 0\\
0 & d_1 & 0 & 0 & 0 & d_1 & 0 & 0\\
0 & 0 & d_1 & 0 & 0 & 0 & d_1 & 0\\
(a_2)_1 & 0 & 0 & 0 & (a_1)_1 & 0 & 0 & 0\\
0 & (b_2)_1 & 0 & 0 & 0 & (b_1)_1 & 0 & 0\\
0 & 0 & (c_2)_1 & 0 & (c_3)_1 & 0 & (c_1)_1 & 0\\
0 & 0 & (c_2)_1 & 0 & (c_3)_1 & 0 & (c_1)_1 & 0\\
0 & (d_4)_1 & 0 & (d_2)_1 & 0 & (d_3)_1 & 0 & (d_1)_1
\end{bmatrix}\begin{bmatrix}
\delta v_0\\ \delta p_0\\ \delta t_0\\ \delta m_0\\ \delta v_1\\ \delta p_1\\ \delta t_1\\ \delta m_1
\end{bmatrix}$$

$$\begin{bmatrix}
1 & 0 & 0 & 0 & 0 & 0 & 0 & 0\\
0 & 1 & 0 & 0 & 0 & 0 & 0 & 0\\
0 & 0 & 1 & 0 & 0 & 0 & 0 & 0\\
0 & 0 & 0 & 1 & 0 & 0 & 0 & 0\\
(a_3)_1 & (a_5)_1 & (a_7)_1 & 0 & 0 & 0 & 0 & 0\\
0 & (b_3)_1 & 0 & (b_5)_1 & 0 & 0 & 0 & 0\\
0 & 0 & (c_5)_1 & 0 & 0 & 0 & 0 & 0\\
0 & 0 & 0 & 0 & 0 & 0 & 0 & 0
\end{bmatrix}\begin{bmatrix}
\delta u_1\\ \delta g_1\\ \delta s_1\\ \delta z_1\\ \delta v_2\\ \delta p_2\\ \delta t_2\\ \delta m_2
\end{bmatrix} = \begin{bmatrix}
(r_1)_{1-(1/2)}\\ (r_2)_{1-(1/2)}\\ (r_3)_{1-(1/2)}\\ (r_4)_{1-(1/2)}\\ (r_5)_{1-(1/2)}\\ (r_6)_{1-(1/2)}\\ (r_7)_{1-(1/2)}\\ (r_8)_{1-(1/2)}
\end{bmatrix} \quad (75)$$

For *j = 1*, we have $[A_1][\delta_1] + [C_1][\delta_2] = [r_1]$. Similar procedures are followed at the different stations. Effectively the seven linearized finite difference equations have the the matrix-vector form:

$$\mathbf{\Lambda\delta_j = \zeta_j} \quad (76)$$

Where $\boldsymbol{\Lambda}$ = Keller coefficient matrix of order 8 x 8, $\boldsymbol{\delta_j}$ = eighth order vector for errors (perturbation) quantities and $\boldsymbol{\zeta_j}$= seventh order vector for *Keller residuals*. This system is then recast as an *expanded matrix-vector system*, viz:

$$\mathbf{\varsigma_j\delta_j - \omega_j\delta_j = \zeta_j} \quad (77)$$

where now $\boldsymbol{\varsigma_j}$ = coefficient matrix of order 8 x 8, $\boldsymbol{\omega_j}$ = coefficient matrix of order 8 x 8 and $\boldsymbol{\zeta_j}$= seventh order vector of errors (iterates) at previous station on grid. Finally the complete linearized system is formulated as a **block matrix system** where each element in the coefficient matrix is a matrix itself. Accurate results are produced by performing a mesh sensitivity analysis. η_{max} has been set at 1 and this defines an adequately large value at which the prescribed boundary conditions are satisfied. It is worth mentioning that throughout the computations, this convergence criterion is used as it is efficient, suitable and the best yet for all the problems considered. Calculations are stopped when

$$\left|\delta v_0^i\right| < \varepsilon_1 \quad (78)$$

Where ε_1 is a small prescribed value, in this study $\varepsilon_1 = 0.0001 \text{ or } 10^{-5}$, that gives about four decimal places accuracy for most predicated quantities as suggested in Cebeci and Bradshaw [32] and also by Bég *et al.* [40, 41].

4. VALIDATION WITH SMOOTHED PARTICLE HYDRODYNAMICS (SPH)

To verify the accuracy of the **KBM** algorithm described above, we also employ a robust **SPH**

algorithm to solve the same boundary value problem defined by eqns. (14-20). **SPH** is a mesh-less particle-based Lagrangian fluid dynamics simulation technique, in which the fluid flow is represented by a collection of discrete elements or pseudo-particles. It was introduced originally for astrophysical fluid dynamics simulations in the late 1970s [42]. It was then further developed for shock gas dynamics and free surface hydrodynamics problems in the 1980s and 1990s by Monaghan and co-workers [43-46]. It has also been applied to viscous-dominated (low Reynolds) number flows [47], ocean hydrodynamics [48], manufacturing fluid mechanics [49], transient pipe flows [50], porous media diffusion [51] and thermal conduction heat transfer [52]. Very recently SPH has been applied to simulate splashdown problems for spacecraft landing modules [53], magnetohydrodynamic porous media thermal convection flows for electro-conductive polymer processing [54] and wavy surface solar collector heat transfer [55]. A good review of modern applications is given in [56]. In comparison to the Eulerian-based conventional numerical methods, SPH has several distinct advantages, which make it particularly adaptable to nonlinear heat transfer, porous media flows and other branches of viscous fluid dynamics. Within the SPH formulation, the computational domain is discretized by a finite set of interpolating points (particles) with invariant coordinates in the material frame. The SPH particles represent a finite mass of the discretized continuum and carry the information about all physical variables which are evaluated at their positions. Although many modifications of SPH have been made in recent years, the foundation for using this technique in a generalized three-dimensional fluid domain, is the three-dimensional Dirac delta function, $\delta^3(x_{ij}^{\beta})$ [56] which satisfies the following identity:

$$f(x_i^{\beta}) = \iiint_{\Omega} f(x_i^{\beta})\delta^3(x_{ij}^{\beta})d\Omega \tag{79}$$

The appropriate two-dimensional form is used in the present study, where $\{f(x_i^{\beta})\}$ is the kernel approximation of the scalar field $f(x_i^{\beta})$ at particle *i.* In SPH the function values and their derivatives at a specific particle are interpolated from the function values at surrounding particles using the interpolating (smoothing) function and its derivatives, respectively:

$$f_i = \sum_j \frac{m_j}{\rho_j} f_j W(\left|r_i - r_j\right|, h \tag{80}$$

$$\nabla_i f_i = \sum_j \frac{m_j}{\rho_j} f_j \nabla_i W(\left|r_i - r_j\right|, h \tag{81}$$

where m is the mass, ρ is the density and W is the interpolating (smoothing) function with a continuous derivative $\nabla_i W$. The index i, j respectively, denotes the variables at the particle i, j respectively, and ∇_i denotes a derivative according to $\boldsymbol{r}_i$ which is the position vector. The smoothing function W is defined so that its value monotonically decreases as the distance between particles increases. It has a compact support domain, for which the radius is defined by the smoothing length h. The smoothing function is normalised and in the limit case, when the smoothing length goes to zero, the smoothing function becomes the Dirac delta function, defined for the general 3-D fluid domain in eqn. (79). Within this study, we have implemented the well-tested and robust *cubic B-spline* smoothing function. Other important aspects of **SPH** are the imposition of an *artificial viscosity* and *artificial stress*. The former is applied in order to smooth the unphysical numerical oscillations, which can arise even in steady-state convection heat transfer. Artificial viscosity is defined as a combination of terms analogous to bulk and von Neumann-Richtmyer viscous pressures which are traditionally used in finite difference methods. The artificial viscosity contains terms with constant artificial viscosity parameters, shear and the bulk viscosity and also a special term to mitigate particle "inter-penetration". The artificial stress term acts as a repulsive force between particles which is elevated when the separation between particles decreases. This is achieved *via* a suitable scaling function, defined as a ratio of the smoothing function values for the actual distance between the pair of particles and the initial particle spacing. In the current model, numerical tests were conducted to establish computational spatial dependence on the number of SPH particles used. Typically computations do not exceed tens of seconds on an Octane SG Desk workstation. The tolerance level was also set, as in the **KBM** simulations, at $\varepsilon = 10^{-7}$. Tables **1-6** depict the comparisons of solutions obtained by both **KBM** and **SPH** for skin friction and wall heat transfer gradient distributions. The correlation is excellent. Confidence in the **KBM** simulations is therefore justifiably very high. The negative velocity values in the tables indicate flow reversal i.e. backflow of both the fluid phase and the particles which are caused in these cases to flow in the downward direction through the channel. Positive values are also computed in particular for the fluid phase (plasma) velocity (Table **2**) at greater transverse coordinate

Table 1: Comparison of Keller Box (KBM) and SPH solutions for fluid-phase velocity U(η) and particle-phase velocity $U_p(\eta)$ values for various Grashof and Darcy number values with transverse coordinate η and Pr = 25, Sk_m = Sk_T = 0.5, B = Ω = 0.1, P_L = γ = Λ = 1.0

Gr	Da	Transverse Coordinate η							
		0.25		0.25		0.5		0.5	
		U(η) KBM	$U_p(\eta)$ KBM	U(η) SPH	$U_p(\eta)$ SPH	U(η) KBM	$U_p(\eta)$ KBM	U(η) SPH	$U_p(\eta)$ SPH
20	0.1	-0.25250	-0.10909	-0.25251	-0.10910	-0.00973	-0.12650	-0.00974	-0.12651
	0.5	-0.30551	-0.10952	-0.30550	-0.10953	-0.01637	-0.12668	-0.01638	-0.12669
	1.0	-0.31394	-0.10960	-0.31393	-0.10961	-0.01786	-0.12672	-0.01787	-0.12673
	10.0	-0.32201	-0.10967	-0.32202	-0.10967	-0.01945	-0.12676	-0.01946	-0.12677
	100.0	-0.32285	-0.10968	-0.32286	-0.10969	-0.01962	-0.12677	-0.01963	-0.12676
100	0.1	-1.23296	-0.11575	-1.23295	-0.11576	-0.00974	-0.12696	-0.00975	-0.12695
	0.5	-1.47915	-0.11745	-1.47914	-0.11746	-0.01639	-0.12722	-0.01640	-0.12723
	1.0	-1.51705	-0.11771	-1.51703	-0.11772	-0.01788	-0.12727	-0.01789	-0.12726
	10.0	-1.55290	-0.11797	-1.55291	-0.11798	-0.01947	-0.12732	-0.01948	-0.12731
	100.0	-1.55659	-0.11799	-1.55658	-0.11798	-0.01965	-0.12733	-0.01964	-0.12732

Table 2: Comparison of Keller Box (KBM) and SPH solutions for fluid-phase velocity U(η) and particle-phase velocity $U_p(\eta)$ values for various Grashof and Darcy number values with transverse coordinate η and Pr = 25, Sk_m = Sk_T = 0.5, B = Ω = 0.1, P_L = γ = Λ = 1.0

Gr	Da	Transverse Coordinate η							
		0.75		0.75		1.0		1.0	
		U(η) KBM	$U_p(\eta)$ KBM	U(η) SPH	$U_p(\eta)$ SPH	U(η) KBM	$U_p(\eta)$ KBM	U(η) SPH	$U_p(\eta)$ SPH
20	0.1	0.23711	-0.15576	0.23710	-0.15575	0.00000	-0.20000	0.00000	-0.20000
	0.5	0.28056	-0.15558	0.28055	-0.15559	0.00000	-0.20000	0.00000	-0.20000
	1.0	0.28686	-0.15556	0.28685	-0.15557	0.00000	-0.20000	0.00000	-0.20000
	10.0	0.29266	-0.15555	0.29265	-0.15556	0.00000	-0.20000	0.00000	-0.20000
	100.0	0.29325	-0.15554	0.29324	-0.15555	0.00000	-0.20000	0.00000	-0.20000
100	0.1	1.21755	-0.14967	1.21754	-0.14968	0.00000	-0.20000	0.00000	-0.20000
	0.5	1.45417	-0.14832	1.45418	-0.14833	0.00000	-0.20000	0.00000	-0.20000
	1.0	1.48993	-0.14813	1.48992	-0.14814	0.00000	-0.20000	0.00000	-0.20000
	10.0	1.52351	-0.14794	1.52350	-0.14795	0.00000	-0.20000	0.00000	-0.20000
	100.0	1.55301	-0.14632	1.55302	-0.14633	1.52695	-0.14793	0.00000	-0.20000

(η = 0.75). Positive values are also particularly evident for fluid phase velocity at lower particle loading parameter values (B = 0.1, 1) at all values of momentum Stokes number (Tables **3** and **4**) and negativity is only observed for very high B value (= 10). The clinical implication of this is that the gravity effect (B) is a critical parameter dictating the direction of the bulk plasma flow in actual auto-transfusion filtration devices. Density of suspensions, therefore, plays a significant role in determining the performance of these medical devices in for example dialysis, as does the plasma viscosity, both characteristics appearing in the mathematical definition of the parameter, B.

Table 3: Comparison of Keller Box (KBM) and SPH solutions for fluid-phase velocity U(η) and particle-phase velocity $U_p(\eta)$ values for various momentum Stokes (Sk_m) and gravity (B) numbers with transverse coordinate η and Pr = 25, Gr = 20, Da = 0.1, Sk_T = 0.5, B = Ω = 0.1, P_L = γ = Λ = 1.0

B	Sk_m	Transverse Coordinate η							
		0.25		0.25		0.5		0.5	
		U(η) KBM	$U_p(\eta)$ KBM	U(η) SPH	$U_p(\eta)$ SPH	U(η) KBM	$U_p(\eta)$ KBM	U(η) SPH	$U_p(\eta)$ SPH
0.1	0.1	-0.25621	-0.90684	-0.25620	-0.90683	-0.01161	-0.92532	-0.01160	-0.92534
	1.0	-0.24807	-0.01168	-0.24806	-0.01167	-0.00754	-0.02774	-0.00753	-0.02773
	10.0	-0.18991	0.05369	-0.18990	0.05368	0.01748	0.05736	0.01749	0.05734
1	0.1	-0.34054	-9.74015	-0.34053	-9.74016	-0.11885	-9.70321	-0.11886	-9.70320
	1.0	-0.32263	-0.76137	-0.32262	-0.76138	-0.10123	-0.72858	-0.10124	-0.72859
	10.0	-0.22247	0.04165	-0.22246	0.04166	-0.01903	0.06611	-0.01904	0.06612
10	0.1	-1.18385	-98.0732	-1.18384	-98.0733	-1.19125	-97.4820	-1.19126	-97.4821
	1.0	-1.06825	-8.25824	-1.06827	-8.25825	-1.03814	-7.73691	-1.03815	-7.73692
	10.0	-0.54800	-0.07874	-0.54801	-0.07875	-0.38410	0.15366	-0.38411	0.15367

Table 4: Comparison of Keller Box (KBM) and SPH solutions for fluid-phase velocity U(η) and particle-phase velocity $U_p(\eta)$ values for various momentum Stokes (Sk_m) and gravity (B) numbers with transverse coordinate η and Pr = 25, Gr = 20, Da = 0.1, Sk_T = 0.5, B = Ω = 0.1, P_L = γ = Λ = 1.0

B	Sk_m	Transverse Coordinate η							
		0.75		0.75		1.0		1.0	
		U(η) KBM	$U_p(\eta)$ KBM	U(η) SPH	$U_p(\eta)$ SPH	U(η) KBM	$U_p(\eta)$ KBM	U(η) SPH	$U_p(\eta)$ SPH
0.1	0.1	0.23794	-0.95616	0.23795	-0.95617	0.00000	-1.00000	0.00000	-1.00000
	1.0	0.23603	-0.05516	0.23604	-0.05517	0.00000	-0.10000	0.00000	-0.10000
	10.0	0.21697	0.04906	0.21698	0.04907	0.00000	-0.01000	0.00000	-0.01000
1	0.1	0.15361	-9.78947	0.15362	-9.78948	0.00000	-10.0000	0.00000	-10.0000
	1.0	0.16146	-0.80487	0.16147	-0.80488	0.00000	-1.00000	0.00000	-1.00000
	10.0	0.18441	0.03697	0.18442	0.03698	0.00000	-0.10000	0.00000	-0.10000
10	0.1	-0.68970	-98.1225	-0.68971	-98.1226	0.00000	-100.000	0.00000	-100.000
	1.0	-0.58417	-8.30195	-0.58418	-8.30196	0.00000	-10.0000	0.00000	-10.0000
	10.0	-0.14121	-0.08390	-0.14122	-0.08391	0.00000	-1.00000	0.00000	-1.00000

Table 5: Comparison of Keller Box (KBM) and SPH solutions fluid-phase velocity U(η) and particle-phase velocity $U_p(\eta)$ values for various particle loading (P_L) and viscosity ratio (Λ) parameters with transverse coordinate η and Pr = 25, Gr = 20, Da = 0.1, Sk_T= Sk_m= 0.5, B = Ω = 0.1, γ = 1.0

P_L	Λ	Transverse Coordinate η							
		0.25		0.25		0.5		0.5	
		U(η) KBM	$U_p(\eta)$ KBM	U(η) SPH	$U_p(\eta)$ SPH	U(η) KBM	$U_p(\eta)$ KBM	U(η) SPH	$U_p(\eta)$ SPH
0.1	0.1	-0.24791	-0.01530	-0.24792	-0.01531	-0.00063	0.01372	-0.00064	0.01371
	1.0	-0.24815	-0.10895	-0.24816	-0.10896	-0.00100	-0.12628	-0.00101	-0.12629
	5.0	-0.24819	-0.12165	-0.24820	-0.12166	-0.00104	-0.14506	-0.00105	-0.14507
1	0.1	-0.25010	-0.01589	-0.25011	-0.01588	-0.00620	0.01272	-0.00622	0.01273
	1.0	-0.25250	-0.10909	-0.25251	-0.10908	-0.00973	-0.12650	-0.00974	-0.12651
	5.0	-0.25283	-0.12169	-0.25284	-0.12167	-0.01020	-0.14511	-0.01021	-0.14512
10	0.1	-0.26654	-0.02067	-0.26655	-0.02069	-0.05169	0.00445	-0.05168	0.00446
	1.0	-0.28533	-0.11022	-0.28534	-0.11023	-0.07924	-0.12828	-0.07925	-0.12829
	5.0	-0.28776	-0.12193	-0.28777	-0.12194	-0.08278	-0.14549	-0.08279	-0.14548

Table 6: Comparison of Keller Box (KBM) and SPH solutions fluid-phase velocity U(η) and particle-phase velocity $U_p(\eta)$ values for various particle loading (P_L) and viscosity ratio (Λ) parameters with transverse coordinate η and Pr = 25, Gr = 20, Da = 0.1, Sk_T= Sk_m= 0.5, B = Ω = 0.1, γ = 1.0

P_L	Λ	Transverse Coordinate η							
		0.75		0.75		1.0		1.0	
		U(η) KBM	$U_p(\eta)$ KBM	U(η) SPH	$U_p(\eta)$ SPH	U(η) KBM	$U_p(\eta)$ KBM	U(η) SPH	$U_p(\eta)$ SPH
0.1	0.1	0.24686	-0.03504	0.24687	-0.03505	0.00000	-0.20000	0.00000	-0.20000
	1.0	0.24658	-0.15558	0.24659	-0.15559	0.00000	-0.20000	0.00000	-0.20000
	5.0	0.24654	-0.17097	0.24655	-0.17098	0.00000	-0.20000	0.00000	-0.20000
1	0.1	0.23979	-0.03591	0.23978	-0.03592	0.00000	-0.20000	0.00000	-0.20000
	1.0	0.23711	-0.15576	0.23712	-0.15578	0.00000	-0.20000	0.00000	-0.20000
	5.0	0.23676	-0.17101	0.23677	-0.17102	0.00000	-0.20000	0.00000	-0.20000
10	0.1	0.17878	-0.04327	0.17879	-0.04329	0.00000	-0.20000	0.00000	-0.20000
	1.0	0.15773	-0.15719	0.15774	-0.15718	0.00000	-0.20000	0.00000	-0.20000
	5.0	0.15507	-0.17132	0.15508	-0.17131	0.00000	-0.20000	0.00000	-0.20000

5. RESULTS AND INTERPRETATION

Extensive computations using KBM are shown in Figures **3-12**.

Figures **3, 4** illustrate the influence of Darcy number, *Da*, on particle velocity and fluid and particle (erythrocyte) temperatures. In medical filter devices, large permeability regimes are used to ensure accelerated flux of the biofluids. Artificial kidneys also exhibit extremely large permeabilities and therefore in the simulations $Da \geq 0.1$. There is a requirement for high permeability porous media in dialysis systems and bio-hemo-filters since a sparse packing of the porous matrix avoids stagnation zones in the flow and also mitigates flow reversal phenomena while sustaining a filtration of the blood fluid-particle suspension. Inspection of the transformed fluid phase momentum equation demonstrates that the Darcian drag, $-\frac{1}{Da}U$ is inversely proportional to Darcy number, the latter being directly proportional to the hydraulic conductivity i.e. permeability, of the porous medium. Darcian drag force is therefore inversely proportional to permeability. With increasing Da the porous medium permeability in the channel is progressively elevated. In the limit as $Da \to \infty$, the porous media fibres disappear and the regime becomes a purely fluid-particle suspension in the vertical channel. As Da is increased particle phase velocities (Figure **3**) which remain always negative across the entire channel span (i.e. reversal of erythrocyte motions is strong, with a net downward flow in the channel), are consistently increased with increasing Darcy number. Particle phase velocity distributions exhibit a monotonic decay from the left channel wall to the right. The permeability parameter,

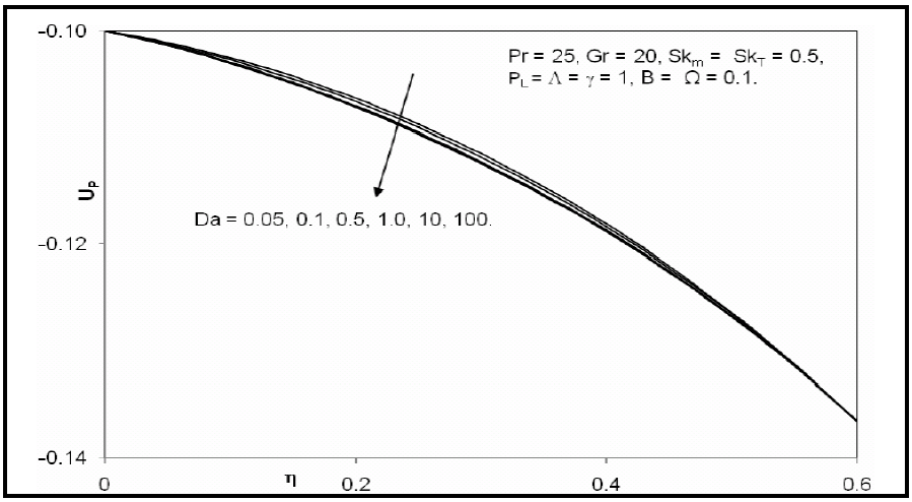

Figure 3: Particle phase velocity distributions for various Darcy numbers.

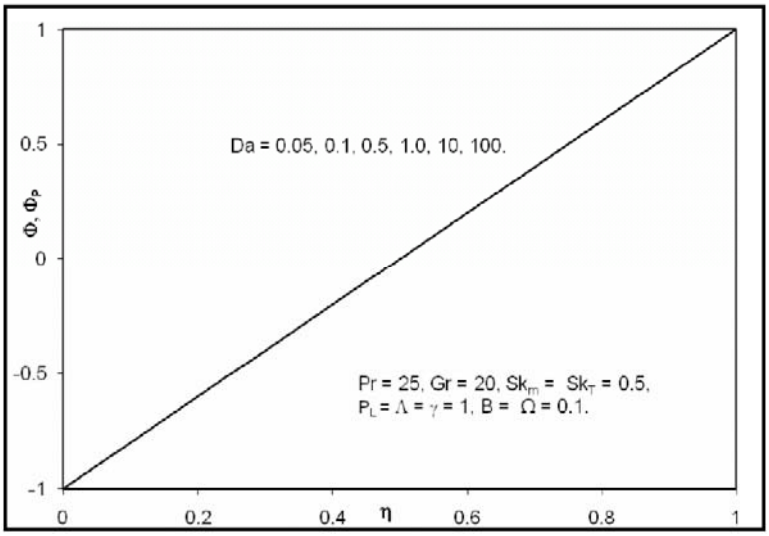

Figure 4: Fluid and particle phase temperature distributions for various Darcy numbers.

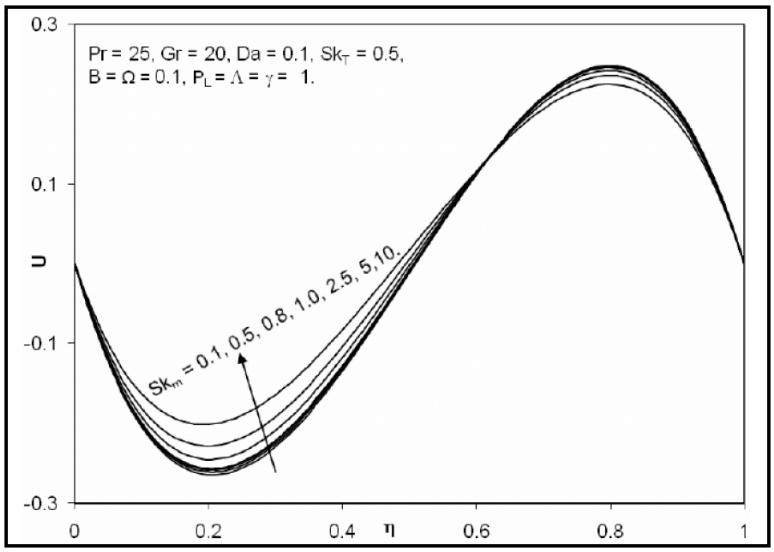

Figure 5: Fluid phase velocity distributions for various momentum Stokes numbers.

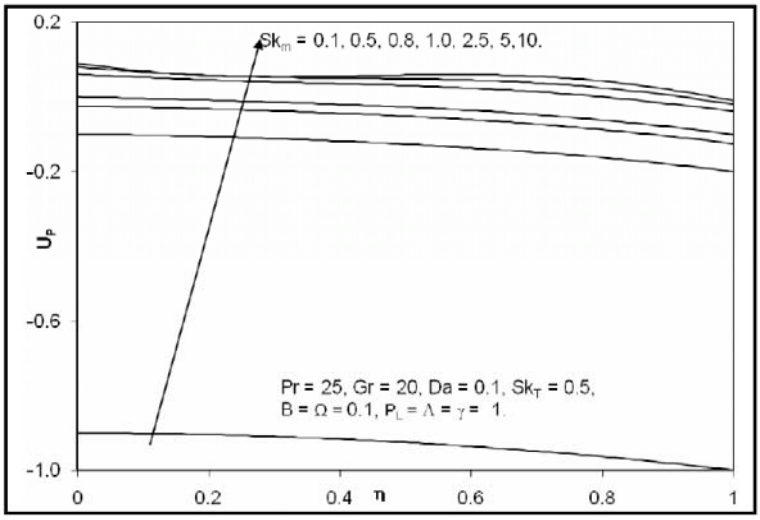

Figure 6: Particle phase velocity distributions for various momentum Stokes numbers.

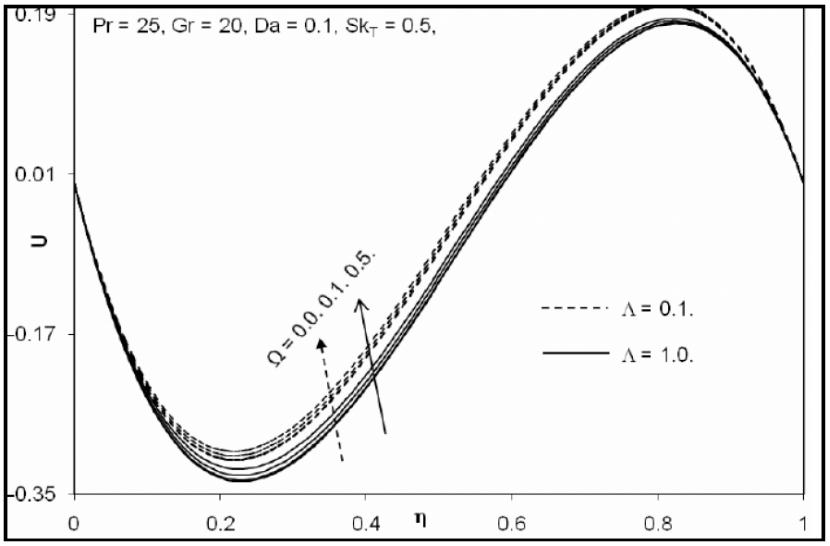

Figure 7: Fluid phase velocity distributions for various particle-phase wall slip and viscosity ratio parameters.

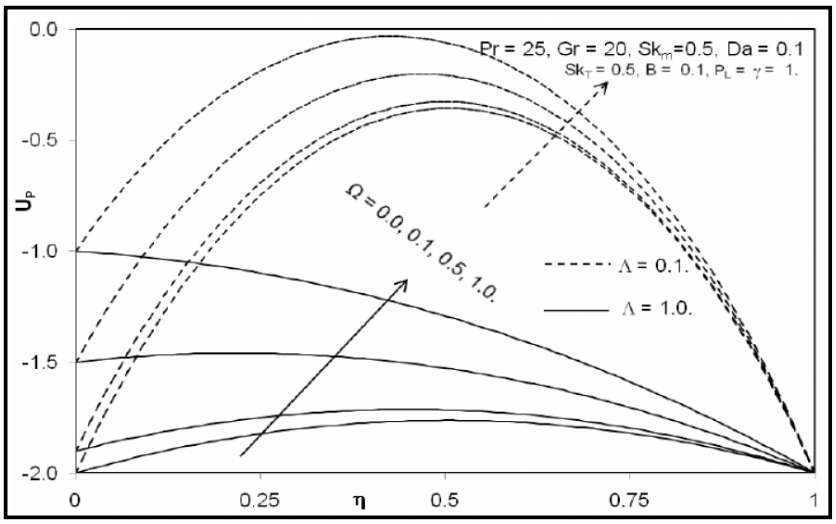

Figure 8: Particle phase velocity distributions for various particle-phase wall slip and viscosity ratio parameters.

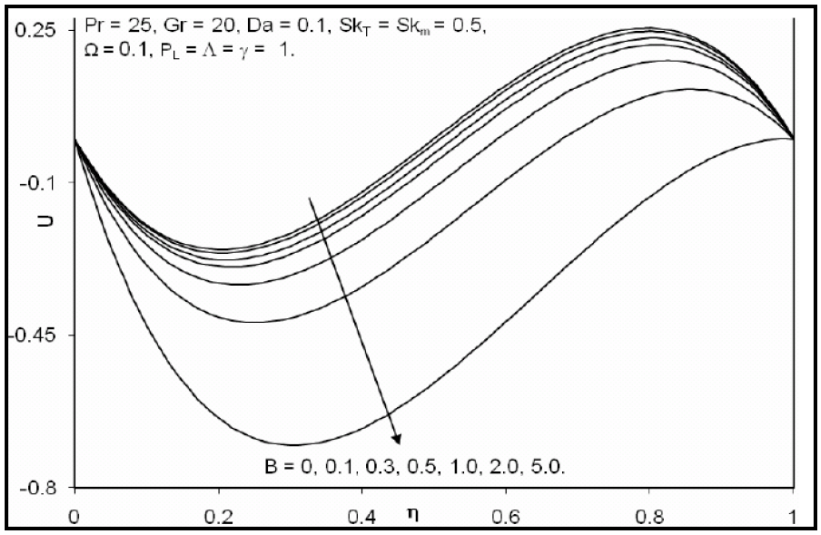

Figure 9: Fluid phase velocity distributions for various gravity parameters.

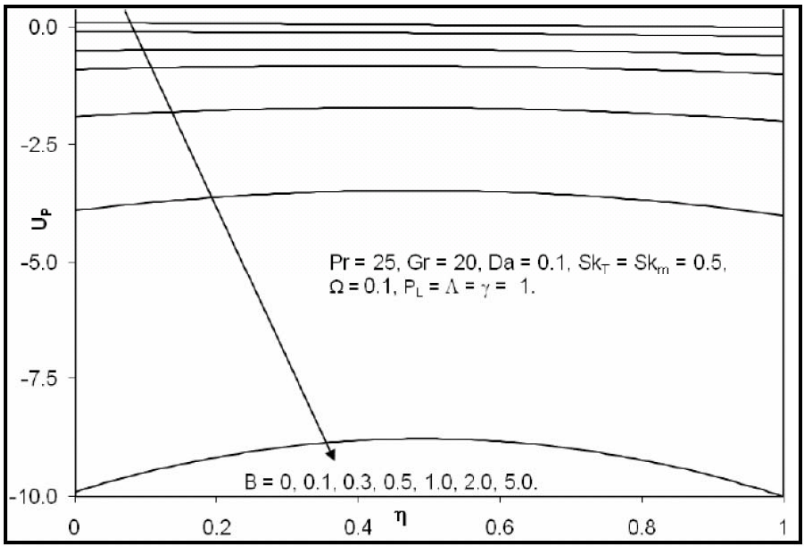

Figure 10: Particle phase velocity distributions for various gravity numbers.

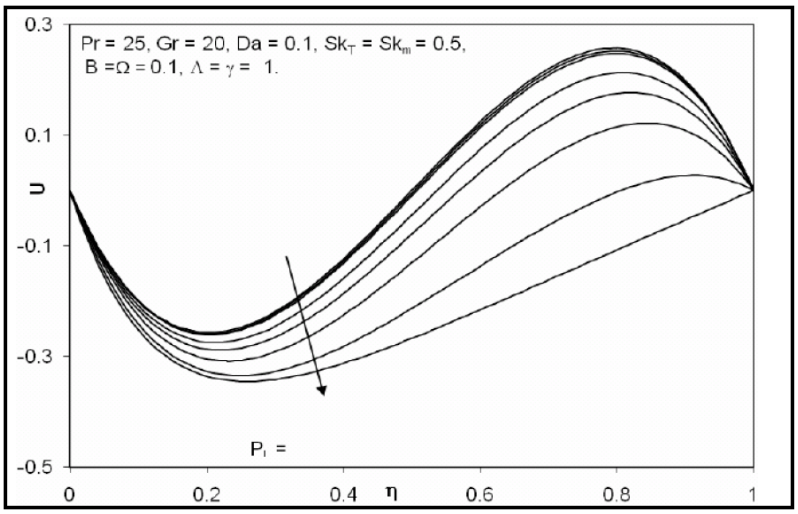

Figure 11: Fluid phase velocity distributions for various particle loading numbers.

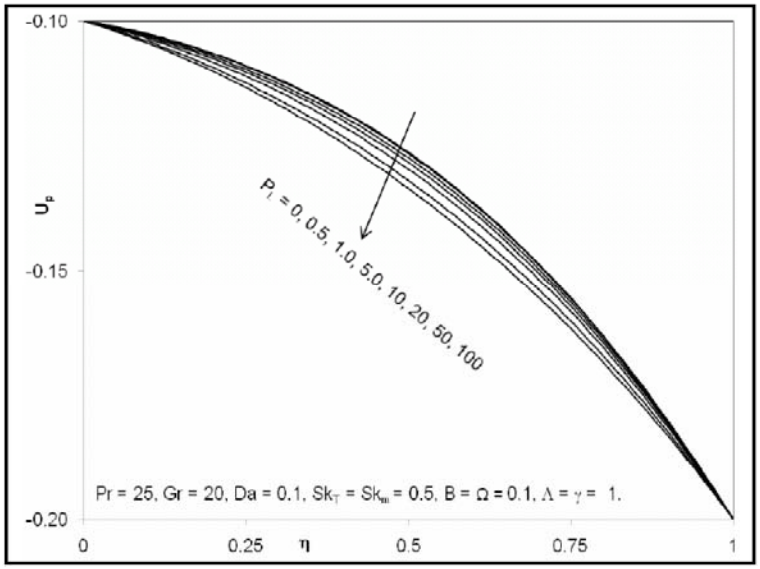

Figure 12: Particle phase velocity distributions for various particle loading numbers.

Da, has an important implication in real clinical systems. As the most widely used blood purification method, hemodialysis serves as a replacement for renal detoxification and discharge functions in the event of chronic kidney failure. The patient's blood is routed *via* a vessel access point by means of a blood pump through a bloodline system into the dialyser (artificial kidney) or in the auto-tranfusion system in the hybrid filter device. This is where the blood is cleaned. The blood flows through the dialyser's capillaries, while the dialyser liquid is bypassed outside the capillary walls in the direction opposing the flow of blood. The primary transport mechanism during hemodialysis is *selective diffusion*. However thermal buoyancy has been explored as an important control mechanism. The presence of the porous medium allows permeation by small and medium-sized molecules and water, but not by large molecules, e.g. proteins. This eliminates toxic substances, restores normal concentrations of other substances (e.g. electrolytes such as potassium, sodium and calcium), balances the blood pH value and removes excess water which has accumulated in the body. While individual substances are eliminated mainly by diffusion, the water is filtered by the porous medium fibers and into the dialyser liquid (ultra-filtration). Alternatives for this include semi-permeable walls, however a combination may prove even more effective. Figure **4** shows that Darcy number has no tangible influence on temperatures of the plasma or the blood cells. This is as expected since the Darcy number is a hydrodynamic effect not a thermal one.

Figures **5** and **6** depict the influence of the inverse momentum Stokes number (Sk_m) on the fluid phase velocity distribution. The parameter, Sk_m, signifies the coupling between the fluid and the particle phases *via* the interphase momentum transfer coefficient (N), the latter being a quantification of relaxation time. Increasing Sk_m will serve to enhance the transfer of momentum from the fluid phase to the particle phase and will effectively decelerate the fluid phase (plasma) velocities-U will therefore be increased i.e. values will become less negative, as observed in Figure **5**. Backflow is therefore also depressed with increasing Sk_m values. Once again we note the oscillatory pattern of fluid phase velocities in which backflow is maximized in the left channel half space and strongly eliminated in the right channel half space. The parameters N and N_T which feature in the inverse momentum Stokes number (Sk_m) and inverse temperature Stokes number (Sk_T), respectively, are measures of relaxation times. Particle phase velocity is also considerably enhanced with an increase in the inverse momentum Stokes number. This parameter features not only in the fluid phase momentum equation *via* the term $(Sk_m)p_L(U\text{-}U_p)$, but additionally arises in the particle phase momentum equation in the term, $(Sk_m)(U\text{-}U_p)$; as such, Sk_m will exert a significant effect on particle phase dynamics.

Figures **7** and **8** show the effect of dimensionless particle-phase wall slip parameter (Ω), and viscosity ratio (Λ) is featured only in the boundary conditions (19), (20). As described earlier, the parameter, Ω, i.e. the dimensionless particle-phase wall slip parameter, simulates the effects of wall slip on the flow and heat transfer in the regime. Increasing Ω values will mobilize an enhanced degree of slip between the particles and the biofluid plasma. As such this parameter is physically important in hameotological processing devices. It is clear that with an increasing of Ω values of $U(\eta)$ and $U_p(\eta)$ are both increased i.e. values are progressively made *less negative*. The undulating fluid phase velocity distribution is evident in Figure **7**, where once again positive flow is only achieved in mainly the channel right half-space; everywhere else there is significant *backflow*. Maximum particle phase velocities (Figure **8**) are computed approximately at the channel vertical centerline and magnitudes are significantly greater than for the fluid phase. In both Figures **7** and **8** as viscosity ratio is *decreased*, both plasma (fluid) and erythrocyte (particle) phase velocities are enhanced i.e. become less negative. Viscosity ratio only features in the particle momentum conservation equation (16). The profiles for Λ *=0.1 are therefore always above those for* Λ *=1.0.*

Figures **9** and **10** depict the response of both fluid and particle phase velocities to a change in the gravity parameter, *B.* This parameter is inversely proportional to dynamic fluid viscosity and directly proportional to the fluid density. It is distinct from the thermal buoyancy parameter, *Gr*. Although both these “gravitational” parameters feature in the fluid phase momentum equation (8), the gravity parameter, B also arises in the particle phase momentum equation (10), the latter as $+B$. In the plasma (fluid) momentum eqn. (14), B arises in the negative body force term, $-P_L B$ where it is coupled with the particle loading parameter, $P_L = \rho_p/\rho$. *The body force* $– P_L B$, acts in a similar fashion to the Darcian porous medium drag force. It will consequently exert a major *inhibiting* effect on both plasma (fluid phase) and particle phase velocity distributions (erythrocytes). This is indeed testified to by the profiles in Figures **9** and **10** where in both cases a strong retardation in velocity phases is induced with increasing B values. Simultaneously there is a dramatic alteration in both sets of profiles. The fluid phase profiles are consistently oscillatory patterns for all B values whereas the particle velocity distributions evolve

from linear profiles to weakly parabolic ones for maximum *B.* The linear particle phase profiles are transformed to an inverted parabola also symmetrical about the channel centerline as *B* values increase. In both cases we have studied the strong free convection case i.e. *Gr* =20, as this is the scenario of greatest interest in bio-thermally-driven hameo-filtration dialysis devices.

Figures **11, 12** illustrate the evolution of fluid and particle phase velocities across the channel with a variation in the particle loading parameter, $P_L = \rho_p/\rho$. This parameter signifies the ratio of the densities of the particle and fluid phases. With a rise in P_L, particle phase density is elevated and this will act to depress the fluid phase velocity magnitudes, as observed in Figure **11**. In this figure clearly the maximum fluid phase velocity corresponds to the weakest particle loading parameter (p_L = 0.05 for which the particle phase density is 5% of the fluid phase density), and the minimum (most negative) fluid phase velocity arises for the strongest particle loading parameter case (p_L = 100) for which the fluid phase density is 100% of the particle phase density i.e. the densities are equal). Very dense biofluid suspensions therefore even under strong buoyancy forces (*Gr* = 20) lead to a significant deceleration in the upward flow in the porous media biofiltration medium. This is an important limiting factor in the design and specification of physiological fluids for such devices. Similarly the fluid phase response, the particle phase velocities are also significantly depressed with a rise in particle loading parameter, owing to the escalation in density of particles which inhibits the motions of the particles in an upward buoyant flow. Backflow of particles is therefore considerably accentuated with an increase in values of P_L.

6. CONCLUSIONS

Keller box finite difference numerical solutions have been presented for the nonlinear, coupled fluid-particle suspension flow and heat transfer in a biofiltration porous media device. The physically realistic case corresponding to a Prandtl number of 25 has been studied which represents accurately laminar heat-conducting blood flow. The present computations have shown that flow is accelerated with increasing Darcy number, corresponding to progressively more permeable regimes. Increasing particle loading parameter decelerates both fluid and particle phase velocities inducing considerable flow reversal and particle motion back-tracking. Increasing gravity parameter decelerates both fluid and particle phase velocities. Increasing particle-phase wall slip parameter manifests with a strong accentuation in both plasma (fluid) and erythrocyte (particle) velocities. However with increasing viscosity ratio both fluid and particle velocities are significantly depressed. The present model has ignored micro-structural rheological effects in blood. These will be simulated using a micropolar hydrodynamic model and the results of these investigations will be communicated imminently. Furthermore the versatility and exceptional accuracy of both Keller box difference and smoothed particle hydrodynamic algorithms in multi-phase hemodynamics has also been clearly demonstrated and it is envisaged that other researchers will apply these methods to biophysical fluid modelling problems.

NOMENCLATURE

Dimensional Parameters

ρ = density of fluid phase

t = time

∇ = gradient operator vector

V = fluid phase velocity vector

P = hydrodynamic pressure

μ = dynamic viscosity of biofluid phase (plasma)

ρ_p = density of particle phase (erythrocytes)

N = interphase momentum transfer coefficient

V_p = particle phase velocity vector

g = gravitational acceleration

K^* = permeability of porous medium

c = specific heat of fluid phase at constant pressure (isobaric)

T = temperature of fluid phase

K = thermal conductivity of fluid phase

c_p = specific heat of particle phase at constant pressure (isobaric)

N_T = interphase heat transfer coefficient

T_p = temperature of particle phase

μ_p = dynamic viscosity of particle phase

x = direction parallel to channel

y = direction transverse to channel

u = velocity of fluid phase

u_p = velocity of particle phase

β^* = coefficient of volumetric expansion

s = separation of plates comprising channel

ω = particle phase wall-slip coefficient

Non-Dimensional Parameters

η = transformed y coordinate

U = dimensionless η-direction fluid phase velocity

U_p = dimensionless η-direction particle phase velocity

Φ = *dimensionless temperature of fluid phase*

Φ_p = dimensionless temperature of particle phase

Da = Darcy number

Pr = fluid phase Prandtl number

γ = specific heat ratio

Sk_T = inverse temperature Stokes number

Sk_m = inverse hydrodynamic (momentum) Stokes number

P_L = particle loading parameter

B = gravity parameter

Λ = viscosity ratio

Gr = Grashof number

Ω = dimensionless particle-phase wall slip parameter

REFERENCES

[1] Jung JH, Hassanein A, Lyczkowski RW. Hemodynamic computation using multiphase flow dynamics in a right coronary artery. Ann Biomed Eng 2006; 34: 393-407. http://dx.doi.org/10.1007/s10439-005-9017-0

[2] Sharan M, Popel AS. A two-phase model for flow of blood in narrow tubes with increased effective viscosity near the wall. Biorheology 2001; 38: 415-28.

[3] Alt W, Dembo M. Cytoplasm dynamics and cell motion: two-phase flow models. Math Biosci 1999; 156: 207-28. http://dx.doi.org/10.1016/S0025-5564(98)10067-6

[4] Sharana M, Pope AS. A two-phase model for flow of blood in narrow tubes with increased effective viscosity near the wall. Biorheology 2001; 38: 415-28.

[5] Cokelet GR, Goldsmith HL. Decreased hydrodynamic resistance in the two-phase flow of blood through small vertical tubes at low flow rates. In Giants of Engineering Science, Chapter 3, Richard Skalak and Biofluid Engineering Science, Matador, UK 2003.

[6] Pries AR, Secomb TW, Gaehtgens P. Biophysical aspects of blood flow in the microvasculature. Microvasc Res 1996; 32: 654-67.

[7] Larson RG, Scriven LE, Davis HT. Percolation theory of two phase flow in porous media. Chem Eng Sci 1981; 36: 57-73. http://dx.doi.org/10.1016/0009-2509(81)80048-6

[8] Adler PM, Brenner H. Multiphase flow in porous media. Ann Rev Fluid Mech 1988; 20: 35-59. http://dx.doi.org/10.1146/annurev.fl.20.010188.000343

[9] Brenner H. Dispersion Resulting from flow through spatially periodic porous media. Phil Trans R Soc Lond A 1980; 297: 81-133. http://dx.doi.org/10.1098/rsta.1980.0205

[10] Marble FE. Dynamics of dusty gases. Ann Rev Fluid Mech 1970; 2: 397-446. http://dx.doi.org/10.1146/annurev.fl.02.010170.002145

[11] Bég OA, Rawat S, Bhargava R. Two-phase magneto-heat transfer in a particle-suspension with heat source and buoyancy effects. International Conference on Advances in Modeling, Optimization and Computing (AMOC-2011), Technical Session M-2: Computational Fluid Dynamics, Indian Institute of Technology (Roorkee), India, December 5-7, 2011.

[12] Bég TA, Rashidi MM, Bég OA, Rahimzadeh N. Differential transform semi-numerical simulation of biofluid-particle suspension flow and heat transfer in non-Darcian porous media. Comput Methods Biomech Biomed Engin 2013; 16: 896-907. http://dx.doi.org/10.1080/10255842.2011.643470

[13] Massoudi M, Kim J, Antaki JF. Modeling and numerical simulation of blood flow using the Theory of Interacting Continua. Int J Non Linear Mech 2012; 47: 506-20. http://dx.doi.org/10.1016/j.ijnonlinmec.2011.09.025

[14] Turcotte DL, Durlofsky L. A triangle based mixed finite element—finite volume technique for modeling two–phase flow through porous media. J Comput Phys 1993; 105: 252-66. http://dx.doi.org/10.1006/jcph.1993.1072

[15] Douglas J Jr. Finite difference methods for two-phase incompressible flow in porous media. SIAM J Numer Anal 1983; 20: 681-96. http://dx.doi.org/10.1137/0720046

[16] Tung VX, Dhir VK. Finite element solution of multi-dimensional two-phase flow through porous media with arbitrary heating conditions. Int J Multiph Flow 1990; 16: 985-1002. http://dx.doi.org/10.1016/0301-9322(90)90103-P

[17] Dzwinel W, Boryczko K, Yuen DA. A discrete-particle model of blood dynamics in capillary vessels. J Colloid Interface Sci 2003; 258: 163-73. http://dx.doi.org/10.1016/S0021-9797(02)00075-9

[18] Sankar S, Lee U. Two-phase non-linear model for the flow through stenosed blood vessels. J Mech Sci Tech 2007; 4: 678-89.

[19] Bourantas GC, Skouras ED, Loukopoulos VC, Burganos VN. Two-phase blood flow modeling and mass transport in the human aorta. in: Biomedical Engineering- 10th International Workshop, Thessalonika, Greece, 5-7 Oct, 2011.

[20] Federspiel WJ. Pulmonary diffusing capacity: implications of two-phase blood flow in capillaries. Resp Physiol 1989; 77: 119-34. http://dx.doi.org/10.1016/0034-5687(89)90035-2

[21] Jaffrin MY, Ding L, Laurent JM. Simultaneous (thermal) convective and diffusive mass transfer in a hemodialyzer. ASME J Biomech Eng 1990; 112: 212-9. http://dx.doi.org/10.1115/1.2891174

[22] Prasad VR, Vasu B, Bég OA. Numerical study of mixed bioconvection in porous media saturated with nanofluid and containing oxytactic micro-organisms. J Mech Med Biol 2013; 13: 25.

[23] Bég OA. Smoothed particle hydrodynamics (SPH) simulation of leukocyte deformation in blood flow. Technical Report-BIO-H-451, 62 pages, Gort Engovation-Aerospace Research, Bradford, UK, July, 2013.

[24] Kedem O, Katchalsky A. Thermodynamics analysis of the permeability of biological membranes to non-electrolytes. Biochim Biophys Acta 1958; 27: 229-46. http://dx.doi.org/10.1016/0006-3002(58)90330-5

[25] Sano Y, Nakayama A. A porous media approach for analyzing a counter current dialyzer system. ASME J Heat Transfer 2012; 134: 072602.1-11.

[26] Drew DA. Mathematical modeling of two-phase flow. Ann Rev Fluid Mech 1983; 15: 261-91. http://dx.doi.org/10.1146/annurev.fl.15.010183.001401

[27] Bég OA, Zueco J, Takhar H.S. Laminar free convection from a continuously moving vertical surface in a thermally-stratified, non-Darcian high-porosity medium: Network numerical study. Int Comm Heat Mass Transfer 2008; 35: 7, 810-6. http://dx.doi.org/10.1016/j.icheatmasstransfer.2008.03.007

[28] Bég OA, Takhar HS, Soundalgekar VM, Woo G. Hydrodynamic and heat-mass transfer modeling of a non-Newtonian fluid through porous medium with boundary effects: numerical simulation. 2nd Int. Conf. on Computational Heat and Mass Transfer, Rio De Janeiro, Brazil, October 22-26, 2001.

[29] Bég OA, Zueco J, Ghosh SK. Unsteady natural convection of a short-memory viscoelastic fluid in a non-Darcian regime: network simulation. Chem Eng Commun 2010; 198: 172-90. http://dx.doi.org/10.1080/00986445.2010.499842

[30] Bég OA, Makinde OD. Viscoelastic flow and species transfer in a Darcian high-permeability channel. J Petrol Sci Eng 2011; 76: 93-9. http://dx.doi.org/10.1016/j.petrol.2011.01.008

[31] Bég OA, Rashidi MM, Rahimzadeh N, Bég TA, Hung T-K. Homotopy semi-numerical simulation of two-phase thermal haemodynamics in a high permeability blood purification device. J Mech Med Biol 2013; 13: 1350066.1-26.

[32] Cebeci T, Bradshaw P. Momentum Transfer in Boundary Layers, Academic Press, New York 1977.

[33] Cebeci T, Bradshaw P. Physical and Computational Aspects of Convective Heat Transfer, Springer Verlag, Berlin/New York 1984. http://dx.doi.org/10.1007/978-3-662-02411-9

[34] Ramachandra V, Prasad V, Bhaskar RN, Bég OA. Free convection heat and mass transfer from an isothermal horizontal circular cylinder in a micropolar fluid with Soret/Dufour effects. Fourth International Conference on Fluid Mechanics and Fluid Power, Indian Institute of Technology Madras, Chennai, December 16-18, 2010.

[35] Keller HB. Numerical Solution of Two-Point Boundary Value Problems, SIAM, Philadelphia, USA 1976.

[36] Bég OA. Numerical methods for multi-physical magnetohydrodynamics (sub and supersonic), Chapter 1, 1-110, New Developments in Hydrodynamics Research, Nova Science, New York, September, 2012.

[37] Prasad VR, Vasu B, Bég OA, Parshad R. Unsteady free convection heat and mass transfer in a Walters-B viscoelastic flow past a semi-infinite vertical plate: a numerical study. Thermal Science-International Scientific Journal 2011; 15: S291-S305.

[38] Prasad VR, Subbarao A, Bhaskar RN, Vasu B, Bég OA. Modelling laminar transport phenomena in a Casson rheological fluid from a horizontal circular cylinder with partial slip. P I Mech Eng E-J PRO 2013. http://dx.doi.org/10.1177/0954408912466350

[39] Prasad VR, Vasu B, Bég OA. Thermo-diffusion and diffusion-thermo effects on free convection flow past a horizontal circular cylinder in a non-Darcy porous medium. J Porous Media 2013; 16: 315-34. http://dx.doi.org/10.1615/JPorMedia.v16.i4.40

[40] Bég OA, Takhar HS, Perdikis C, Ram PC. Mathematical Modeling of hydromagnetic convection of a second order fluid in non-Darcy porous media using the Keller-Box difference scheme. Theoretical and Applied Mechanics Conference, Blacksburg, Virginia, USA, June, [Complex Convection Session] 2002.

[41] Bég OA, Prasad VR, Takhar HS, Soundalgekar VM. Thermo-convective flow in an isotropic, homogenous medium using Brinkman's model: Numerical Study. Int J Num Methods Heat Fluid Flow 1998; 8: 59-89. http://dx.doi.org/10.1108/09615539810220298

[42] Lucy LB. A numerical approach to the testing of the fission hypothesis. Astron J 1977; 82: 1013-24. http://dx.doi.org/10.1086/112164

[43] Monaghan JJ, Gingold RA. Shock simulation by the particle method SPH. J Comput Phys 1983; 52: 374-89. http://dx.doi.org/10.1016/0021-9991(83)90036-0

[44] Monaghan JJ. Smoothed particle hydrodynamics. Rep Prog Phys 2005; 30: 1703-59. http://dx.doi.org/10.1088/0034-4885/68/8/R01

[45] Monaghan JJ. Simulating free surface flows with SPH. J Comput Phys 1994; 110: 399-406. http://dx.doi.org/10.1006/jcph.1994.1034

[46] Monaghan JJ. SPH without a tensile instability. J Comput Phys 2000; 159: 290-311. http://dx.doi.org/10.1006/jcph.2000.6439

[47] Morris JP, Fox PJ, Zhu Y. Modeling low Reynolds number incompressible flows using SPH. J Comput Phys 1997; 136: 214-26. http://dx.doi.org/10.1006/jcph.1997.5776

[48] Oger G, Doring M, Alessandrini B, Ferrant P. Two-dimensional SPH simulations of wedge water entries. J Comput Phys 2006; 213: 803-22. http://dx.doi.org/10.1016/j.jcp.2005.09.004

[49] Comas-Cardona S, Groenenboom PHL, Binetruy C, Krawczak P. A generic mixed FE-SPH method to address hydro-mechanical coupling in liquid composite moulding processes. Composites: Part A 2005; 36: 1004-10.

[50] Sigalotti LDG, Klapp J, Sira E, Melean Y, Hasmy A. SPH simulations of time-dependent Poiseuille flow at low Reynolds numbers. J Comput Phys 2003; 191: 622-38. http://dx.doi.org/10.1016/S0021-9991(03)00343-7

[51] Zhu Y, Fox PJ. Smoothed particle hydrodynamics model for diffusion through porous media. Transport Porous Med 2001; 43: 441-71. http://dx.doi.org/10.1023/A:1010769915901

[52] Cleary PW, Monaghan JJ. Conduction modelling using smoothed particle hydrodynamics. J Comput Phys 1999; 148: 235-36. http://dx.doi.org/10.1006/jcph.1998.6118

[53] Bég OA. SPLASH- A smoothed particle hydrodynamic solver for spacecraft "splashdown" simulations in MATLAB. Technical Report for European Space Consortium- AERO-D-61-SPH, Gort Engovation-Aerospace Engineering Sciences, Bradford, UK, 85 pages, July, 2013.

[54] Bég OA. Smoothed particle hydrodynamic simulation of magnetic field materials processing, Technical Report for Metallurgy Industry (Norway)- MANUFACT-M-14-SPH, Gort Engovation-Aerospace Engineering Sciences, Bradford, UK, 64 pages, August, 2013.

[55] Bég OA, Motsa SS, Takhar HS. Pseudo-spectral and smoothed particle hydrodynamic simulation of natural convection from a wavy surface to non-Darcian porous media, Computers Fluids 2013; Submitted.

[56] Liu GR, Liu MB. Smoothed Particle Hydrodynamics: A Meshfree Particle Method, World Scientific Publishing Co., Singapore 2003.

Received on 19-10-2013 Accepted on 3-12-2013 Published on 10-02-2014

DOI: http://dx.doi.org/10.12970/2311-1755.2013.01.02.4